Neural Network–Based Impedance Synthesis for Multi-Probe Harmonic Tuners

G. I. Arenas-Alvarez, *Student Member, IEEE*, J. R. Loo-Yau, *Senior Member, IEEE*, L. M. Aguilar-Lobo, E. A. Hernández-Domínguez, *Member, IEEE*, and J. A. Reynoso-Hernández, *Member, IEEE*

***Abstract*—This work presents a deep neural network (DNN) approach to solve the inverse tuner control problem in multi-probe harmonic impedance tuners used in RF Load-Pull measurements. In this problem, the desired reflection coefficients at the tuner reference plane are specified, and the corresponding probe positions must be determined. The proposed methodology addresses the complex nonlinear interactions inherent in multi-probe systems, where the movement of a single probe shifts the impedance across multiple harmonics, rendering traditional brute-force search methods impractical due to the large number of possible probe configurations. Two feedforward DNN architectures featuring six hidden layers were designed and trained to predict the motor steps required to synthesize target impedances at the tuner reference plane. Experimental validation using a Focus Microwaves iMPT-1818-TC tuner at a 3 GHz fundamental frequency demonstrated prediction accuracies of 96.61% in magnitude and 94.03% in phase. Furthermore, a multi-harmonic model simultaneously controlling 3 GHz and 6 GHz achieved accuracies of 90.15% in magnitude and 87.78% in phase at the fundamental, and 88.12% in magnitude and 74.92% in phase at the second harmonic. By replacing iterative VNA-based searches with a predictive model, the proposed approach significantly reduces tuner pre-characterization time and improves the efficiency of RF transistor Load-Pull measurements.**

Link to graphical and video abstracts, and to code: **https://latamt.ieeer9.org/index.php/transactions/article/view/10737**

***Index Terms*—Deep neural networks, harmonic impedance tuners, impedance synthesis, load-pull measurements, multi-probe tuners, RF measurement automation**

I. Introduction

In the design of RF power amplifiers (PA), the load-pull technique is widely used to evaluate how transistor output power, efficiency, and linearity vary with the presented load impedance. Since its initial publication [1], this technique has evolved from continuous-wave (CW) analysis to advanced characterization scenarios where harmonic terminations play a critical role [2]- [4]. In high-efficiency, continuous-mode designs, accurate second-harmonic control is essential to shape voltage and current waveforms, making harmonic load-pull characterization indispensable.

Load-pull systems are generally classified into passive [5]–[6], active [7]– [8], and hybrid [9] configurations. While active systems rely on signal injection and hybrid systems combine passive tuners with active load modulation, passive mechanical tuners remain the most economical and widely used solution, synthesizing load impedance through mechanically movable, electronically controlled probes.

Extending passive tuners to harmonic frequencies introduces significant complexity. Dedicated tuners per frequency band increase hardware cost [10], while multi-probe tuners reduce hardware requirements but create a highly coupled, nonlinear tuning space due to probe interactions. Furthermore, multiple physical configurations can yield similar impedance values, posing a complex inverse control problem. For high-resolution tuners such as the Focus Microwaves iMPT-1818-TC considered here, an exhaustive search could require years of measurement time, making conventional iterative methods computationally prohibitive.

This work addresses this limitation by formulating multi-probe tuner control as an inverse mapping problem and solving it with deep neural networks (DNNs). Although DNNs have been applied in RF domains such as antenna design [11], filter synthesis [12], and transistor modeling [13], their use for direct inverse prediction of motor positions in a multiprobe harmonic tuner has not been previously reported. The main contributions of this work are as follows. First, the tuner control problem is formulated as a direct inverse mapping, enabling the prediction of motor positions from a target impedance and eliminating the need for iterative Vector Network Analyzer (VNA) based searches. Second, a dataset acquisition and filtering methodology is proposed to mitigate the non-injective behavior of multiprobe harmonic tuners, enabling reliable supervised training in a high-dimensional coupled space. Finally, experimental validation on a commercial Focus Microwaves iMPT-1818-TC tuner demonstrates simultaneous impedance synthesis at 3 GHz and 6 GHz with high prediction accuracy in both magnitude and phase.

II. The Harmonic Impedance Tuner

In RF PA design, the mode of operation is defined by the voltage and current waveforms at the active device, which are strongly influenced by the load impedances presented at the

The associate editor coordinating the review of this manuscript and approving it for publication was Roberto S. Murphy (*Corresponding author: G. I. Arenas-Alvarez*).

This work was supported by the Secretaría de Ciencia, Humanidades, Tecnología e Innovación (SECIHTI), formerly CONAHCYT-México (previously CONACYT-México), under Projects 163272 and 206029.

G. I. Arenas-Alavarez, J. R. Loo-Yau, and E. A. Hernández-Domínguez, are with the Cinvestav, Unidad Guadalajara, Zapopan, México (e-mails: gustavo.arenas@cinvestav.mx, raul.loo@cinvestav.mx, and ernesto.hernandez@cinvestav.mx).

L. M. Aguilar-Lobo is with the Universidad Autónoma de Guadalajara, Zapopan, Jalisco, México (e-mail: lina.aguilar@edu.uag.mx).

J. Apolinar Reynoso-Hernández is with the Centro de Investigación Científica y de Educación Superior de Ensenada, Ensenada, Baja California, México (e-mail: apolinar@cicese.mx).

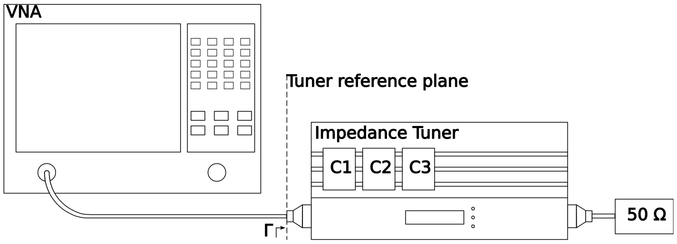

Fig. 1. Measurement setup for the harmonic impedance tuner characterization.

fundamental frequency and its harmonic components [14]. In particular, the second harmonic plays a key role in shaping the waveforms and performance of continuous-mode PAs [15]. As a result, harmonic load-pull characterization requires accurate and efficient control of the impedances presented at multiple frequency components, especially at the second harmonic, placing stringent demands on the performance and usability of harmonic impedance tuners.

A mechanical harmonic impedance tuner can be used to reduce the complexity and cost of harmonic load-pull setups that would otherwise require multiple impedance tuners. Such tuners typically employ a multiprobe structure in which the probes are mutually coupled, so that the movement of a single probe affects the impedances seen at multiple frequencies, including the fundamental and its harmonics. The probes (C1, C2 and C3) are actuated by stepper motors (X and Y) controlled by a computer, and the impedance at the tuner reference plane is typically determined using a vector network analyzer (VNA), as shown in Fig. 1. The motors are driven by computer commands that position the probes to synthesize a desired impedance at the tuner reference plane. During operation, the resulting impedance is measured with the VNA and the probe positions are adjusted until the target load condition is achieved.

In practice, the desired impedance is obtained through an iterative process in which the probes are moved to different positions and the resulting impedances are measured until the target impedance is achieved. This procedure constitutes a pre-characterization of the tuner, during which load-pull measurements on the device under test are not performed.

Furthermore, when the objective is to modify the impedance at a single frequency while maintaining the impedances at the remaining frequencies unchanged, the tuning process becomes significantly more challenging. Due to the interaction between the probes, adjusting one probe alters the impedances across multiple frequency components, which substantially increases the time required to identify the appropriate probe positions.

This non-injective behavior has direct implications for supervised learning. Due to the mutual coupling between probes, different motor position combinations may produce similar or nearly identical impedance values at the tuner reference plane. Consequently, the inverse mapping from impedance to motor position is not unique. In a supervised learning framework, this introduces ambiguity in the training labels. As a result, the DNN may experience degraded convergence, increased prediction variance, and reduced reliability during inference.

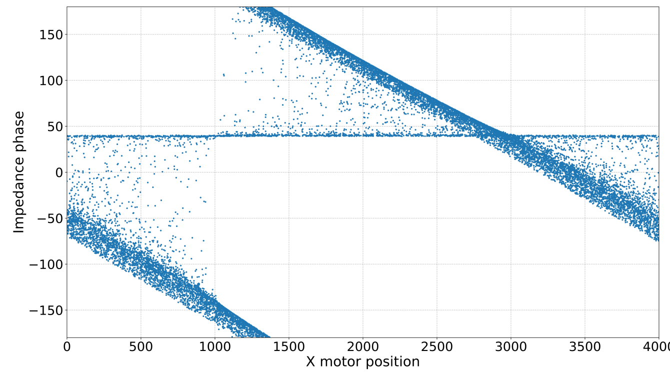

Fig. 2. $\angle\Gamma_{f0}$ vs motor X position of probe C_1.

To mitigate this issue, the dataset is filtered to retain regions where the impedance-to-position mapping is approximately injective, thereby reducing label ambiguity and improving the stability and consistency of the learning process, as described in Section III.

To address this problem, a deep neural network (DNN) is proposed to predict the probe positions required to achieve a target impedance at the tuner reference plane, as described in the following sections. A previous analysis of different conventional and non-neural baselines are summarized in Table I, where their limitations are discussed and the selection of a DNN architecture is based on their capability of nonlinear multivariable mapping, generalization performance, very low time inference, and high efficiency regardless of the training dataset size.

The first step for developing the DNN is the characterization of the impedance tuner to determine how the probe positions affect the impedance at the tuner reference plane for the fundamental frequency and its harmonics. Although the tuner includes three probes, only the first two probes are used in this work in order to focus on the control of the fundamental and second harmonic impedances.

A. Characterization of the Impedance Tuner for a Single Frequency

For a single frequency, this characterization can be performed in a relatively straightforward manner [16]. As an initial approach, a single-frequency scenario with a single-probe is considered. The position of C_1 probe was varied by sweeping the stepper motors controlling the longitudinal position (X motor) from 0 to 20,000 steps and the penetration depth (Y motor) from 0 to 8,950 steps. For each probe position, the impedance at the tuner reference plane was measured using a calibrated VNA [17] at 3 GHz.

To provide insight into the magnitude of possible motor-step combinations, even with only one probe, the total number of combinations is 20,000 × 8,940 = 178,800,000. Even though multiple probe positions may correspond to identical or nearly identical impedance values at the tuner reference plane due to the non-injective nature of the tuner response, the effective search space remains extremely large. Consequently, a brute-force approach is not feasible, as measuring all possible

TABLE I
COMPARISON OF INVERSE TUNER CONTROL METHODOLOGIES

Methodology	Handling of probe coupling	Scalability	Real-time inference cost	Motor position validation MAE
Analytical / parametric models	Cannot account for electromagnetic interaction	Equations become analytically unsolvable	Very low	NA
Polynomial surface regression	Requires independent models per motor	Helicoidal surfaces require high-order polynomials	Low	159.29 - 324.53 at single frequency
K-nearest neighbors (KNN)	Suffers from the "curse of dimensionality" as variables increase	High (requires massive memory and scales with dataset size)	Distance-based interpolation from a stored dataset	45.97 at single frequency 118.76 at dual frequency
Deep neural networks (proposed)	Natively maps highly coupled, multidimensional inputs	Readily scales to higher dimensions with robust generalization	Very low (constant time after training)	12.01 at single frequency 49.88 at dual frequency

combinations would require approximately five years, assuming a measurement time of 1 s per point, which represents an optimistic lower bound and does not include additional overhead such as probe settling time, VNA triggering, or data storage.

Due to the non-injective behavior, repeated impedance values are observed in the dataset. Figs. 2 and 3 show the phase and magnitude of the reflection coefficient Γ_{f_0} of C_1 probe after removing repeated impedance data points. These results reveal the nonlinear interaction between the motor positions and the reflection coefficient Γ at the fundamental frequency, demonstrating that the displacement of each motor simultaneously influences both the magnitude and phase of Γ_{f_0}. A significant variation in $|\Gamma_{f_0}|$ is observed only when motor Y is positioned beyond approximately 5,500 steps (Fig.3); otherwise, the influence of X motor is negligible (Fig.2). Regarding phase control, X motor must be limited to the range of 0 to 4,000 steps to ensure a single phase rotation (–180° to 180°) (Fig. 2); beyond this range, the phase response becomes periodic with respect to motor position, increasing ambiguity and potentially degrading the learning performance of the neural network.

B. Characterization of the Impedance Tuner for Two Frequencies

Continuing with the analysis, the case of two frequencies is studied, in which a sweep of the X and Y motors positions of the first and the second probes (C_1 and C_2) was performed. It is found that the interaction between the probes is significant and more erratic, and the movement of even one motor affects the impedance seen at the reference plane of the tuner for the fundamental frequency (3 GHz) and the second harmonic (6 GHz). This interaction significantly increases the complexity of the impedance control problem. After performing several measurements, the reflection coefficients Γ_{f_0} and Γ_{2f_0} are shown in Figs. 4 and 5, respectively. In these figures, the blue lines represent a fixed X_1 motor position at 1000 steps for both 3 and 6 GHz, while the orange lines represent a fixed distance of 1000 steps between X's motors of C_1 and C_2 probes ($X_2 - X_1 = 1000$ steps). This behavior can be modeled according to the following observations:

- Keeping a fixed distance (motor steps) between the X's motors of the C_1 and C_2 probes constant (orange lines in Figs. 4 and 5), the magnitudes $|\Gamma_{f_0}|$ and $|\Gamma_{2f_0}|$ can be kept relatively constant with a change of 1.89% (3 GHz) and 7.76% (6 GHz), while the phases $\angle\Gamma_{f_0}$ and $\angle\Gamma_{2f_0}$ change between 38.33% and 50.28% at 3 and 6 GHz, respectively.
- If one of the motors X's is fixed (in this case X_1) and the other is moved, the phases $\angle\Gamma_{f_0}$ and $\angle\Gamma_{2f_0}$ move with a lower ratio between 14.37% and 32.88%, and the magnitudes change significantly between 13.18% and 53.78% at 3 and 6 GHz respectively (blue lines in Figs. 4 and 5).

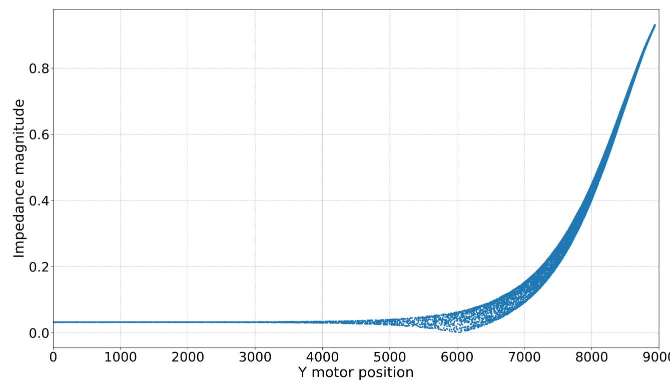

Fig. 3. $|\Gamma_{f0}|$ vs motor Y position of probe C_1.

It is important to mention that Figs. 4 and 5 represent only a part of the X's motor sweep. For the above, it is necessary to use the distance between the X motors of C_1 and C_2 probes, or the value of $X_2 - X_1$ as an input parameter for the DNN. Now it is possible to analyze how much distance (steps) is required to change the phase from -180 to 180 degrees for both frequencies. This is an advantage, since the C_1 probe is limited to the minimum X motor actual position of the C_2 probe due to mechanical constraints of the tuner.

III. DNNs Design and Training

To characterize the behavior of the impedance tuner for one and two frequencies, two DNNs are developed, a single-frequency DNN for targeting impedance control at the fundamental frequency (3 GHz), and a dual-frequency DNN to address simultaneous control at the fundamental and second harmonic (3 and 6 GHz).

The datasets were generated by controlling the motor positions of the probes while measuring the corresponding re-

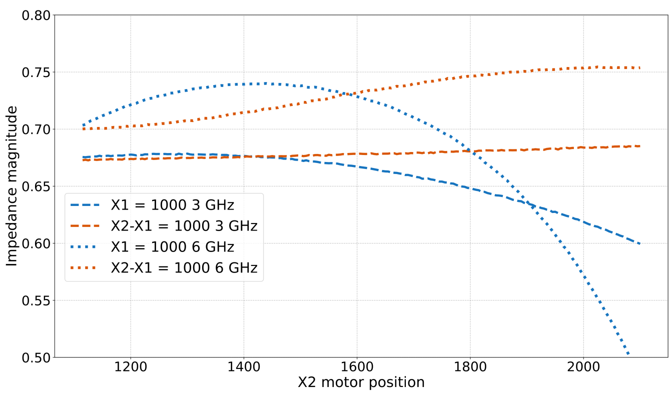

Fig. 4. $|\Gamma|$ vs motor X position of probe C_2.

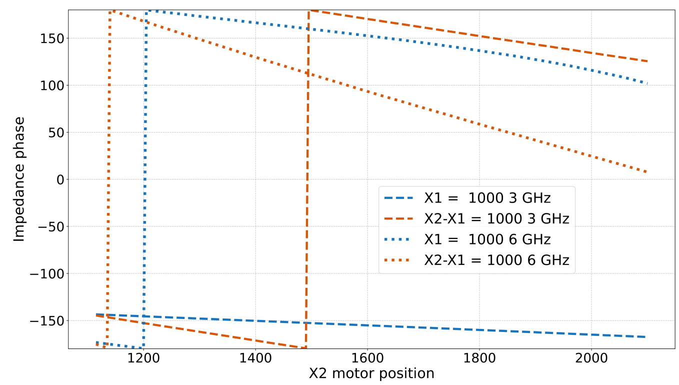

Fig. 5. $\angle\Gamma$ vs motor X position of probe C_2.

flection coefficients using a VNA. Specifically, for the single-frequency network, the dataset was acquired using a uniform distribution of measurement points across the mechanical range established during the initial analysis presented in Section II. Conversely, for the dual-frequency network, a hybrid sampling strategy was implemented: the penetration motors were positioned according to a semi-normal distribution centered on their maximum values, whereas the longitudinal motors were assigned a uniform distribution. The collected data were then filtered to restrict the training domain of the neural networks and promote an approximately injective mapping between impedance values and motor positions.

By constraining the penetration depth and longitudinal range of each probe, regions where multiple probe configurations yield similar impedance values are largely excluded. Within this filtered space, the network learns a single admissible and physically consistent solution rather than an average over multiple valid configurations. This is an important distinction because while other valid probe positions might exist outside the training domain, the predicted solution is expected to lie within a well-behaved region of the tuner response, where the mapping is stable and the predictions are reliable. The trade-off is a reduced coverage of the full impedance plane, which is reflected in the increased error observed near the Smith chart boundary. This filtering directly mitigates the non-injective mapping described in Section II by removing ambiguous training labels associated with multiple valid motor configurations.

For the single-frequency DNN, the longitudinal position (X motor) is limited to 0–4,000 steps, consistent with the single-phase rotation condition identified in Section II-A (Fig. 2), and the penetration depth (Y motor) is constrained above approximately 6,000 steps, where a significant and monotonic variation in $|\Gamma_{f_0}|$ is observed (Fig. 3). This filtering reduces the occurrence of ambiguous impedance-to-position mappings in the training dataset. For the dual-frequency DNN, the dataset is filtered such that the penetration depths (Y motor) of C_1 and C_2 probes are greater than approximately 7000 steps. In addition, the relative distance between the longitudinal positions (X motor) of C_1 and C_2 probes is constrained to the range of approximately 900 to 2500 steps based on the coupled probe behavior described in Section II-B (Figs. 4 and 5). The longitudinal position of C_1 probe (X motor) is limited to the range between 0 and 3800 steps to ensure a single phase rotation at the fundamental frequency. These filtering criteria are based on the analysis of the tuner behavior and are designed to preserve representative tuner responses while minimizing ambiguities in the mapping between probe positions and impedance values.

Once the dataset has been defined, the two DNNs models are designed. Each DNN employs a feedforward architecture, commonly used for regression problems [18] - [19], and is designed with the same basic topology of an input layer, six hidden layers and an output layer. Six hidden layers were selected as a compromise between sufficient model capacity to represent the highly nonlinear tuner response and stable training behavior without significant overfitting. The input layer represents the target impedance using its real and imaginary components together with the normalized values of magnitude and phase. This redundant representation provides complementary information about the impedance distribution and facilitates the learning process by improving the sensitivity of the network to variations in both amplitude and phase. Since the real and imaginary components are inherently bounded between -1 and 1, no additional normalization is applied to these quantities. The normalized magnitude and phase are computed as:

$$\text{Magnitude} = \sqrt{\text{Real}^2 + \text{Imaginary}^2} \tag{1}$$

$$\text{Phase} = \frac{\text{atan2}(\text{Imaginary}, \text{Real})}{\pi} \tag{2}$$

and where the real and imaginary components correspond to the normalized in-phase and quadrature parts of the target reflection coefficient, respectively. It is important to note that the phase, together with the magnitude and the real and imaginary components, is used exclusively as an input feature to the network. The DNN outputs and the corresponding training error are defined entirely in terms of motor step positions, which are continuous physical quantities without circular periodicity. Consequently, the wrapping behavior inherent to angular variables does not affect the training process of the proposed DNNs.

Six hidden layers are used with *tanh* activation function to introduce non-linearity, facilitate convergence during training, maintain bounded activations, and demonstrate better performance compared to other activation functions. The number of neurons in each layer changes for both DNNs. Finally, the output layer provides the normalized values of each motor position (X and Y) required to synthesize the desired impedance at the tuner reference plane for each case. For the single-frequency DNN, there are two outputs (X and Y positions), and for the dual-frequency DNN, there are four outputs (X_1, Y_1, X_2, Y_2 positions). The equations (3) - (6) are used for the denormalization of the output values for each motor of the probes, where (3) and (4) are used for the single-frequency DNN, and (3) - (6) are used for the dual-frequency DNN, defined as:

$$X_{1DNorm} = \mathrm{X}_{1Norm} \times 4000 \tag{3}$$

$$Y_{1DNorm} = \mathrm{Y}_{1Norm} \times 2940 + 6000 \tag{4}$$

$$X_{2-1DNorm} = \mathrm{X}_{2-1Norm} \times 2300 + 700 \tag{5}$$

$$Y_{2DNorm} = \mathrm{Y}_{2Norm} \times 2960 + 7000 \tag{6}$$

Where the subscript Norm denotes the network output before denormalization, and DNorm denotes the resulting motor step value applied to the tuner.

The model parameters (hidden layers and neurons for each layer) were optimized using Bayesian optimization [20]. The Pytorch framework was used for training, and dropout regularization with a rate of 0.5% is applied to mitigate overfitting. Higher values increase the number of epochs to converge because of the large dataset, while 0.5% provides sufficient regularization as confirmed by the close agreement between training and validation errors shown in Figs. 8 and 9. The RAdam optimizer is employed with a learning rate of 0.0005, which is half of the default, and the training process minimizes the mean absolute error (MAE) loss function, using the entire dataset as the batch (full-batch training), which speeds up training. The number of training epochs was selected based on the validation MAE performance, corresponding to the point where no further improvement in prediction error was observed.

A. Single-frequency DNN

Fig. 6 illustrates the architecture of the single-frequency DNN developed for the fundamental frequency. The input layer consists of four neurons corresponding to the magnitude, phase, real and imaginary parts of the reflection coefficient at 3 GHz. This layer is followed by six hidden layers that contain 250, 450, 500, 250, 120, and 40 neurons, respectively. The output layer comprises two neurons to predict the positions of X and Y motors of the C_1 probe.

The dataset used for this case has 13,000 samples and was divided into training, validation and test subsets using an 80%–10%–10% ratio. Therefore, 10,400 samples are used for training, while 1,300 are assigned for both validation and testing. The split was made with random distribution using a seed to replicate the results. The network was trained for 100,000 epochs, requiring approximately 16 minutes on a workstation equipped with an Intel Core i5-10400 CPU, 24 GB of RAM, and an NVIDIA RTX 4060Ti GPU. The reported training time is provided as a reference and may vary depending on the computational resources used.

B. Dual-frequency DNN

The dual-frequency DNN designed to operate at the fundamental and second-harmonic frequencies has the architecture shown in Fig. 7. The input layer consists of eight neurons, corresponding to the magnitude, phase, real and imaginary components of the reflection coefficient at 3 and 6 GHz. This is followed by six hidden layers with 350, 550, 600, 350, 200, and 60 neurons, respectively. The output layer comprises four neurons to predict the longitudinal position (X_1) and penetration depth (Y_1) of C_1 probe, the longitudinal separation between the X motors of C_1 and C_2 probes ($X_2 - X_1$), and the penetration depth (Y_2) of C_2 probe.

In this case, the dataset is significantly larger due to the increased number of possible probe-position combinations, as discussed previously. A total of 271,005 samples are used, divided into training, validation, and test sets comprising 90%, 9%, and 1% of the dataset, respectively using the same seed for reproducibility. This corresponds to 243,905 samples for training, 24,390 for validation, and 2,710 for testing. The network was trained for 200,000 epochs, requiring approximately 9 hours to complete the training using the same computational resources described in the previous subsection.

IV. Experimental Results

This section presents the experimental results obtained to evaluate the performance of both proposed DNNs for impedance synthesis using an iMPT 1818-TC multiharmonic impedance tuner. The objective of these experiments is to assess the capability of the single-frequency and dual-frequency DNNs to accurately predict the required X and Y motors positions of the tuner probes as a function of the target reflection coefficients defined at the tuner reference plane. The validation is performed by comparing the target reflection coefficients with the reflection coefficients measured after applying the motor positions predicted by the DNNs. Furthermore, repeated inference experiments confirmed that the neural networks produce consistent and identical motor position predictions for the same impedance target, demonstrating the deterministic stability of the proposed approach.

A. Metrics of Training Process of the DNNs

The training results for both DNNs are considered satisfactory. For the single-frequency DNN, the mean absolute error (MAE) is 10.94 motor steps for the training set, and 12.01 motor steps for the validation set, indicating a close agreement between the predicted and target motor positions. For the dual-frequency DNN, the MAE increases to 29.31 motor steps for the training set and 49.88 motor steps for the validation set. This increase is expected due to the higher complexity of the problem, as multiple probes and frequency components are controlled simultaneously. The validation values are compared in Table I as a reference to the performance of other baseline

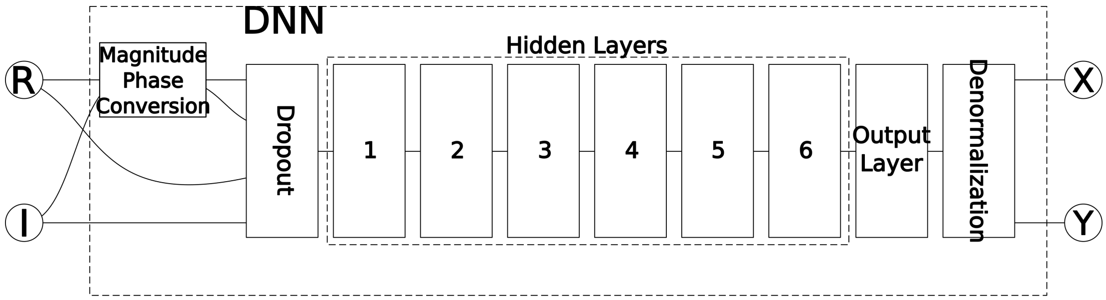

Fig. 6. Architecture of the DNN at f_0.

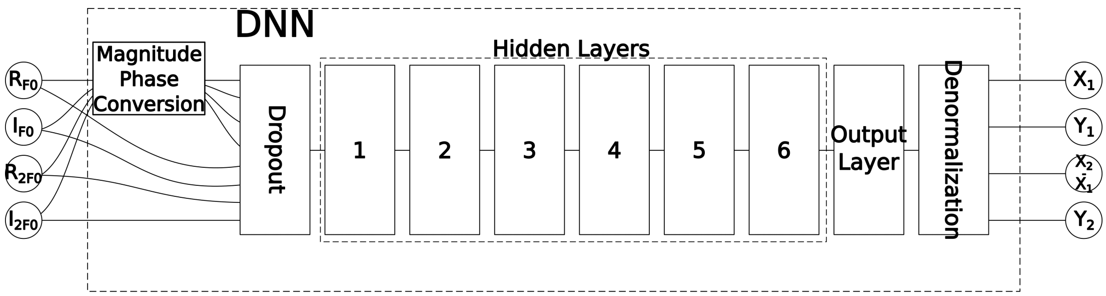

Fig. 7. Architecture of the DNN at $2f_0$.

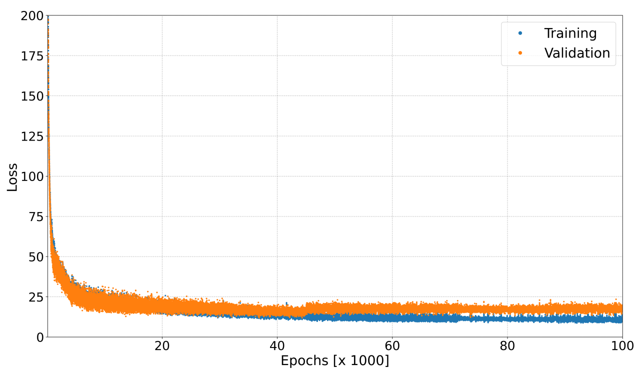

Fig. 8. Training curves of the DNN at f_0.

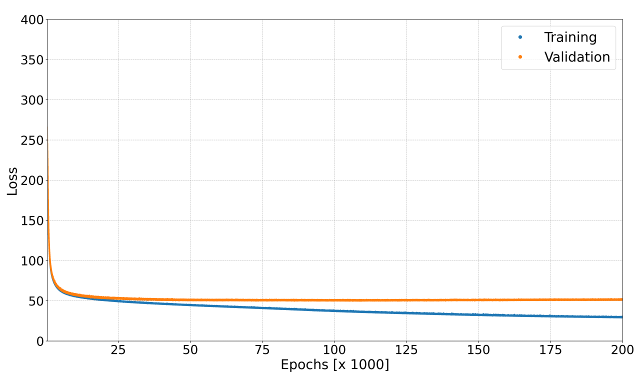

Fig. 9. Training curves of the DNN at $2f_0$.

methods. The DNNs demonstrate superior performance in terms of prediction accuracy, generalization capability, and inference speed compared to conventional approaches.

Figs. 8 and 9 show the training curves for the single-frequency and the dual-frequency DNNs, respectively, where the loss function (MAE) decreases consistently with the number of epochs for both training and validation sets. This behavior indicates stable convergence and the absence of overfitting during training.

The generalization capability of the models is further validated using the test sets. The single-frequency DNN achieves a test MAE of 16.64 motor steps, while the dual-frequency DNN reaches 48.68 motor steps. These values are consistent with the corresponding validation errors, confirming that both DNNs generalize well to unseen data.

B. *Single-frequency DNN Prediction*

For the single-frequency DNN, two experimental tests are performed at 3 GHz to evaluate its ability to predict the motor positions required to achieve a target impedance at the tuner reference plane. In the first test, a set of desired impedance points, randomly selected within the impedance region covered by the training dataset and excluded from the training and validation sets, is defined on the Smith chart. For each target impedance, the motor positions (X, Y) predicted by the DNN are sent to the tuner, and the resulting impedance is measured using the VNA and compared against the target to evaluate the accuracy of the predictions, in terms of magnitude and phase of the reflection coefficient. The corresponding results are summarized in Table II. In this table, the relative error is computed with respect to the target magnitude and phase, respectively, while the General MAE quantifies the overall prediction error directly in the complex plane, that is, the average absolute difference between the target and measured complex reflection coefficients, reported independently from the Magnitude MAE and Phase MAE. The prediction accuracy is defined as 100% minus the relative error, providing an intuitive measure of model performance. Fig. 10 shows the

TABLE II
DNN TEST RESULTS AT f_0

Test number	Test 1	Test 2
Mesh points	1200	1072
General MAE (Γ_{f0})	0.01129	0.01252
Magnitude MAE ($\lvert\Gamma_{f0}\rvert$)	0.00903	0.01134
Phase MAE ($\angle\Gamma_{f0}$)	2.89752°	1.40686°
Magnitude Relative Error	3.39%	2.17%
Phase Relative Error	5.97%	2.68%

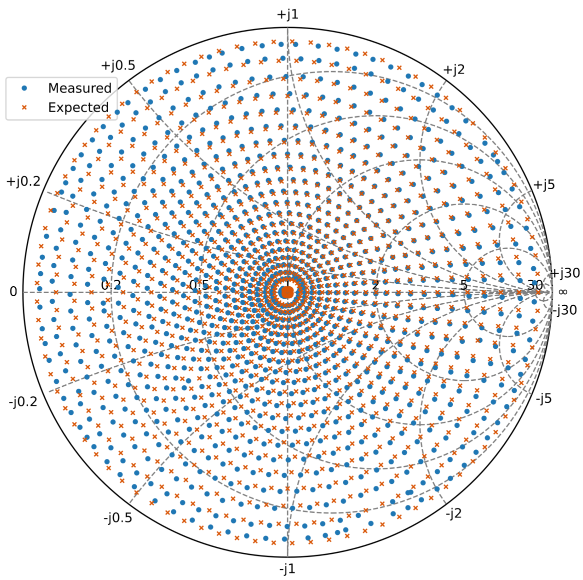

Fig. 10. Desired and measured impedances for the DNN test 1 at f_0.

comparison between the desired and measured impedances on the Smith chart.

In the second test, the distribution of the target impedances is different, focusing on a specific region of the Smith chart, then the same measurement procedure is followed. This test evaluates the single-frequency DNN performance when the target impedances are concentrated in a specific region of the Smith chart. The results of this test are also reported in Table II, and the corresponding desired and measured impedances are shown in Fig. 11. The results of both tests cases demonstrate that the single-frequency DNN can accurately predict the motor positions, showing the robustness of the model across different regions of the Smith chart.

C. Dual-frequency DNN Prediction

To test the dual-frequency DNN that control the fundamental and the second harmonic, a set of desired impedances is defined simultaneously at the fundamental frequency (3 GHz) and the second harmonic (6 GHz), and the dual-frequency DNN is used to predict the motor steps required to achieve these impedances. In Fig. 12, the desired impedances are shown on a Smith chart for both frequencies. Identical impedance meshes are defined at the fundamental frequency and the second harmonic. Since the dual-frequency DNN simultaneously controls both impedances, each impedance point of the mesh at the fundamental frequency is associated

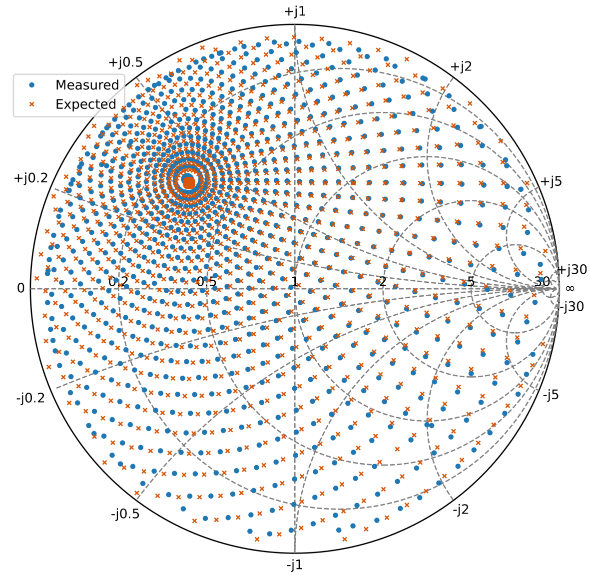

Fig. 11. Desired and measured impedances for the DNN test 2 at f_0.

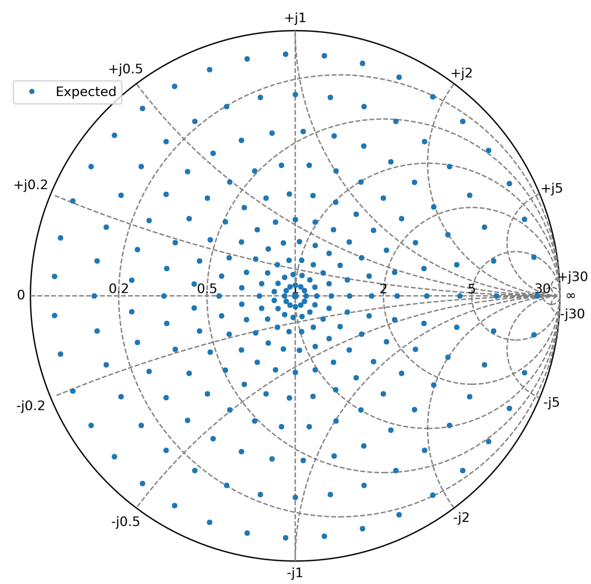

Fig. 12. Impedance mesh for the two harmonics DNN test.

with a corresponding point at the second harmonic, resulting in a total of 76,176 impedance combinations. The results of the test are shown in Table III.

A test scenario was designed to evaluate the dual-frequency DNN harmonic decoupling capability. In this experiment, the impedance at the fundamental frequency is kept fixed at a specific target point, while the second harmonic is programmed to perform a phase sweep maintaining a constant reflection coefficient magnitude ($|\Gamma_{2f_0}|$). This procedure was repeated for three different magnitude levels to cover various regions of the Smith chart.

The results of this test are presented in Figs. 13 and 14. Fig. 13 illustrates the stability of the fundamental frequency, where the measured reflection coefficients remain clustered

TABLE III
TWO HARMONICS DNN TEST RESULTS

Mesh points	76,176
General MAE (Γ_{f0} and Γ_{2f0})	0.03502
Magnitude MAE ($\lvert\Gamma_{f0}\rvert$)	0.01483
Phase MAE ($\angle\Gamma_{f0}$)	8.81129°
Magnitude Relative Error ($\lvert\Gamma_{f0}\rvert$)	9.85%
Phase Relative Error ($\angle\Gamma_{f0}$)	12.22%
Magnitude MAE ($\lvert\Gamma_{2f0}\rvert$)	0.02133
Phase MAE ($\angle\Gamma_{2f0}$)	15.81142°
Magnitude Relative Error ($\lvert\Gamma_{2f0}\rvert$)	11.88%
Phase Relative Error ($\angle\Gamma_{2f0}$)	25.08%

around the target reflection coefficient $\Gamma_{f_0} = 0.62\angle 120°$. This demonstrates that the dual-frequency DNN effectively compensates for the complex probe interactions inherent to harmonic control. Meanwhile, the accuracy of the trajectories synthesized for the second harmonic, shown in Fig. 14, is quantified using the Mean Squared Error (MSE) between the desired and measured reflection coefficients, expressed in decibels (dB) and annotated in the figure. It can be observed that the measured impedances closely follow the desired trajectories for the second harmonic while maintaining the target point at the fundamental frequency.

However, the prediction error increases as the synthesized impedance approaches the edge of the Smith chart. For magnitudes exceeding 0.7, the tuner behavior becomes more erratic due to the increased tuner sensitivity near the Smith chart boundary. This physical sensitivity is reflected in the Mean Squared Error (MSE), defined as the average squared error between the desired and measured reflection coefficients. The MSE was 0.00514 (-45.77 dB) for the fixed fundamental point. For the second-harmonic phase sweeps, the MSE values shown in Fig. 14 range from -63.52 dB to -29.12 dB for the different magnitudes of $|\Gamma_{2f_0}|$, increasing as the magnitude of the reflection coefficient approaches unity. The increased error in high-magnitude regions is consistent with the behavior expected near the boundary of the training domain, where the density of training samples decreases and the tuner response becomes more sensitive to small variations in probe position. This represents a known limitation of data-driven approaches when operating near or beyond the edges of the training distribution, and will be addressed in future work through data augmentation and improved sampling strategies in high-magnitude regions. The stability of the fundamental point while sweeping the second harmonic phase is critical for accurate Load-Pull characterization, as it ensures that harmonic tuning does not inadvertently alter the fundamental matching conditions.

V. CONCLUSION

Deep neural network (DNN)–based models were developed and experimentally validated to predict the motor positions required to synthesize a target impedance at the reference plane of a harmonic impedance tuner. A single-frequency model at 3 GHz and a dual-frequency model controlling the fundamental and second harmonic (3 and 6 GHz) were developed.

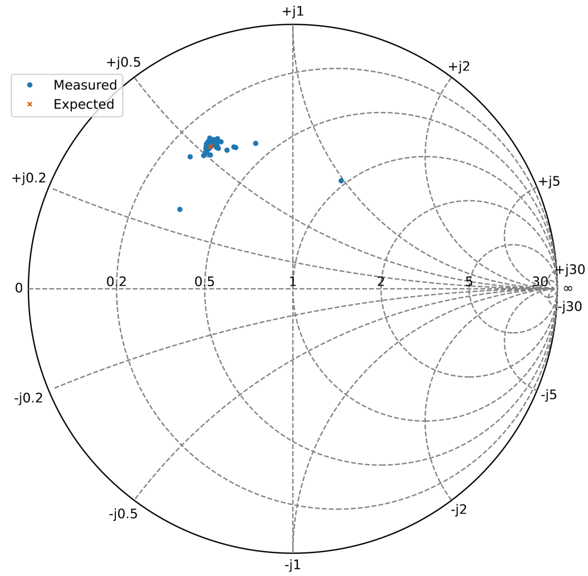

Fig. 13. Desired and measured impedances at f_0 for the two harmonics DNN test.

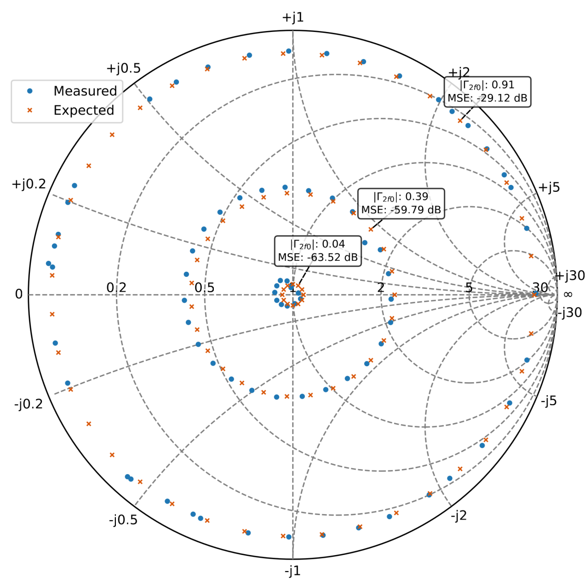

Fig. 14. Desired and measured impedances at $2f_0$ for the two harmonics DNN test.

The results demonstrate that the proposed approach effectively solves the inverse tuner control problem, yielding measured impedances that closely match the desired targets. The single-frequency model achieves high accuracy across most of the impedance plane, whereas the dual-frequency case exhibits increased error, particularly in phase at the second harmonic, due to the higher dimensionality and coupling of the multi-harmonic tuning space. In the experimental validation, the single-frequency model achieved prediction accuracies of 96.61% in magnitude and 94.03% in phase, while the dual-frequency model reached 90.15% in magnitude and 87.78% in phase at the fundamental frequency, and 88.12% in magnitude and 74.92% in phase at the second harmonic. Larger deviations are observed for reflection coefficient magnitudes above approximately 0.7, where the tuner response becomes more sensitive.

This work focuses on the impedance synthesis problem itself; therefore, the impact of the reported impedance deviations on device-specific RF performance metrics such as efficiency, gain, or output power is beyond the scope of this study.

By eliminating exhaustive brute-force searches during tuner characterization, the method significantly reduces setup time. Once trained, predictions are obtained in milliseconds, and the overall measurement time becomes limited primarily by the mechanical motion of the tuner and instrumentation response.

These results demonstrate the practical viability of DNN-based impedance tuning for nonlinear RF measurements. The proposed methodology is not restricted to the frequencies considered here; it can be extended to other frequency bands by repeating the characterization procedure and retraining the DNNs with the corresponding dataset. Future work will extend the methodology to third-harmonic control, investigate the robustness of the approach under measurement uncertainty and experimental perturbations, develop data augmentation and improved sampling strategies for high-magnitude impedance regions, and explore generalized frequency-dependent models capable of operating across multiple frequency bands within a unified framework.

REFERENCES

[1] J. M. Cusack, S. M. Perlow and B. S. Perlman, *"Automatic Load Contour Mapping for Microwave Power Transistors"*, in IEEE Transactions on Microwave Theory and Techniques, vol. 22, no. 12, pp. 1146-1152, Dec. 1974, doi: 10.1109/TMTT.1974.1128456.

[2] F. H. Raab, *"Class-F power amplifiers with maximally flat waveforms"*, in IEEE Transactions on Microwave Theory and Techniques, vol. 45, no. 11, pp. 2007-2012, Nov. 1997, doi: 10.1109/22.644215.

[3] F. H. Raab, *"Class-E, Class-C, and Class-F power amplifiers based upon a finite number of harmonics"*, in IEEE Transactions on Microwave Theory and Techniques, vol. 49, no. 8, pp. 1462-1468, Aug. 2001, doi: 10.1109/22.939927.

[4] S. K. Dhar et al., *"Input-Harmonic-Controlled Broadband Continuous Class-F Power Amplifiers for Sub-6-GHz 5G Applications"*, in IEEE Transactions on Microwave Theory and Techniques, vol. 68, no. 7, pp. 3120-3133, July 2020, doi: 10.1109/TMTT.2020.2984603.

[5] M. Guidry et al., *"W-band passive load pull system for on-wafer characterization of high power density N-polar GaN devices based on output match and drive power requirements vs. gate width"*, 2016 87th ARFTG Microwave Measurement Conference (ARFTG), San Francisco, CA, USA, 2016, pp. 1-4, doi: 10.1109/ARFTG.2016.7501955.

[6] D. Veit, M. Gadringer and E. Leitgeb, *"About Different Load Configurations for Mixed-Mode Load-Pull Measurements"*, 2019 European Microwave Conference in Central Europe (EuMCE), Prague, Czech Republic, 2019, pp. 150-153.

[7] C. J. Clymore et al., *"First Comparison of Active and Passive Load Pull at W-Band"*, 2023 101st ARFTG Microwave Measurement Conference (ARFTG), San Diego, CA, USA, 2023, pp. 1-4, doi: 10.1109/ARFTG57476.2023.10279609.

[8] A. Ben Ayed and S. Boumaiza, *"Millimeter-Wave Wideband Active Load—Pull System Using Vector Network Analyzer Frequency Extenders"*, in IEEE Microwave and Wireless Technology Letters, vol. 35, no. 6, pp. 932-935, June 2025, doi: 10.1109/LMWT.2025.3564839.

[9] K. Lukasik, P. Barmuta, T. Nielsen, K. Madziar, D. Schreurs and A. Lewandowski, *"Hybrid load-pull system using a two-source nonlinear vector network analyzer"*, 2015 Integrated Nonlinear Microwave and Millimetre-wave Circuits Workshop (INMMiC), Taormina, Italy, 2015, pp. 1-3, doi: 10.1109/INMMIC.2015.7330378.

[10] John F. Sevic, *"Automated Impedance Synthesis"*, in *The Load-pull Method of RF and Microwave Power Amplifier Design*, Wiley, 2020, pp.17-43, doi: 10.1002/9781119078128.ch2.

[11] M. Wang, S. Yu, J. Dong, H. Luo and C. Xiao, *"Multiobjective Optimization of Antenna Inverse Design With Data Augmentation Based on K-Means-NN"*, in IEEE Antennas and Wireless Propagation Letters, vol. 24, no. 9, pp. 3144-3148, Sept. 2025, doi: 10.1109/LAWP.2025.3584825.

[12] V. Miraftab and M. Yu, *"Innovative Combline RF/Microwave Filter EM Synthesis and Design Using Neural Networks"*, 2007 International Symposium on Signals, Systems and Electronics, Montreal, QC, Canada, 2007, pp. 1-4, doi: 10.1109/ISSSE.2007.4294399.

[13] H. Luo, X. Yan, J. Zhang and Y. Guo, *"A Neural Network-Based Hybrid Physical Model for GaN HEMTs"*, in IEEE Transactions on Microwave Theory and Techniques, vol. 70, no. 11, pp. 4816-4826, Nov. 2022, doi: 10.1109/TMTT.2022.3206442.

[14] M. El Mahalawy, N. Misljenovic and A. Fayed, *"A load-pull approach using multi-frequency harmonic tuners for enhancing PAE and device model accuracy"*, 2014 IEEE 57th International Midwest Symposium on Circuits and Systems (MWSCAS), College Station, TX, USA, 2014, pp. 603-606, doi: 10.1109/MWSCAS.2014.6908487.

[15] T. B. Mader, E. W. Bryerton, M. Markovic, M. Forman and Z. Popovic, *"Switched-mode high-efficiency microwave power amplifiers in a free-space power-combiner array"*, in IEEE Transactions on Microwave Theory and Techniques, vol. 46, no. 10, pp. 1391-1398, Oct. 1998, doi: 10.1109/22.721140.

[16] C. Roff, J. Graham, J. Sirois and B. Noori, *"A new technique for decreasing the characterization time of passive load-pull tuners to maximize measurement throughput"*, 2008 72nd ARFTG Microwave Measurement Symposium, Portland, OR, USA, 2008, pp. 92-96, doi: 10.1109/ARFTG.2008.4804298.

[17] J. Apolinar Reynoso Hernández; Manuel Alejandro Pulido Gaytan, *"Principles and Applications of Vector Network Analyzer Calibration Techniques"*, River Publishers, 2024, pp.i-xxx., doi: 10.1201/9788770046350

[18] C. Morales Morales et al., *"Digital Artificial Neural Network Implementation on a FPGA for data classification"*, in IEEE Latin America Transactions, vol. 13, no. 10, pp. 3216-3220, Oct. 2015, doi: 10.1109/TLA.2015.7387224.

[19] J. Salas, F. de Barros Vidal and F. Martinez-Trinidad, *"Deep Learning: Current State"*, in IEEE Latin America Transactions, vol. 17, no. 12, pp. 1925-1945, December 2019, doi: 10.1109/TLA.2019.9011537.

[20] B. Shahriari, K. Swersky, Z. Wang, R. P. Adams and N. de Freitas, *"Taking the Human Out of the Loop: A Review of Bayesian Optimization"*, in Proceedings of the IEEE, vol. 104, no. 1, pp. 148-175, Jan. 2016, doi: 10.1109/JPROC.2015.2494218.

G. I. Arenas-Alvarez (Student Member, IEEE) received his B.Sc. degree in electronics and communications engineering from the Escuela Superior de Ingeniería Mecánica y Eléctrica (ESIME), Instituto Politécnico Nacional (IPN), Mexico City, Mexico, in 2016. The M.Sc. degree in electrical engineering from the Centro de Investigación y de Estudios Avanzados del IPN (Cinvestav), Guadalajara Unit, Mexico, in 2025. He is currently pursuing the Ph.D. degree in electrical engineering at the CINVESTAV, Zapopan, Mexico. His research interests include RF and microwave circuit design, with a focus on impedance tuners, load-pull measurements, power amplifier design, and the application of machine learning techniques for RF systems.

J. R. Loo-Yau (Senior Member, IEEE) received his B.S. degree from Universidad Autónoma de Guadalajara, Mexico, in 1998, and the M.Sc. and D.Sc. degrees from CICESE, Mexico, in 2000 and 2006, respectively. In 2007, he joined Cinvestav, Guadalajara, where he is currently the Head of the Electronic Design Group. He has co-authored over 50 peer-reviewed papers. His research team has twice placed in the top three at the IEEE/MTT-S IMS High-Efficiency PA Student Design Competition. Dr. Loo-Yau was a founding member of the IEEE MTT-S Guadalajara Chapter and served on the LAMC organizing committees in 2016 and 2023. Since January 2026, he has served as an Associate Editor for IEEE Transactions on Microwave Theory and Techniques. He is also a reviewer for other international journals. His research focuses on nonlinear modeling of microwave transistors, high-efficiency power amplifiers, and digital predistortion.

L. M. Aguilar-Lobo received her PhD degree in Electrical Engineering with the specialty in Electronic Design from the Centro de Investigación y de Estudios Avanzados del IPN (Cinvestav), Guadalajara Unit, in 2016, and her M.S. degree in Electrical Computer Engineering from the University of Guadalajara. Currently, she is researcher at the Computer Science Department of the Universidad Autónoma de Guadalajara. Her research interests are modeling and linearization of RF power amplifiers, wireless communication systems, real time embedded systems, machine learning, intelligent systems and the applications of the Internet of Things.

E. A. Hernández-Domínguez received his Ph.D. (2024) and M.Sc. (2020) degrees in Electrical Engineering from the Centro de Investigación y de Estudios Avanzados del IPN, Mexico, and the B.Eng. degree in Electronic Design and Intelligent Systems from the Centro de Enseñanza Técnica Industrial in 2018. His research focuses on RF and microwave circuit design, particularly power amplifiers and nonlinear device characterization. His work integrates theory, simulation, and experimental validation, with contributions to RF power amplifiers, reflectionless filters, broadband bias networks, and in-fixture calibration techniques. He has also worked on the optimization of impedance matching networks and RF power amplifiers using metaheuristic algorithms. He is currently involved in academic and industrial collaborations in RF and microwave system design and optimization.

J. A. Reynoso Hernández (Member, IEEE) received his B.Sc. degree in electronics and telecommunications engineering from ESIME, IPN, Mexico City, Mexico, in 1984, the M.Sc. degree from CINVESTAV, IPN, in 1985, and the D.E.A. and Ph.D. degrees from LAAS-CNRS, Université Paul Sabatier, Toulouse, France, in 1987 and 1989, respectively. Since 1990, he has been a Titular Researcher at CICESE, Ensenada, Mexico. He is a member of the Mexican National System of Researchers (SNI, Level II). He is the main author of the book titled “Principles and Applications of Vector Network Analyzer Calibration Techniques” (River Publishers, 2024). His research interests include high-frequency on-wafer measurements, device modeling, and VNA calibration techniques. Dr. Reynoso-Hernández served as an Associate Editor for IEEE Transactions on Microwave Theory and Techniques (2023–2026) and has led CICESE’s Microwave Group to receive five Best Interactive Forum Paper Awards at ARFTG conferences.